RSC Advances

ROYAL SOCIETY OF CHEMISTRY

www.rsc.org/advances

Graphical Abstract

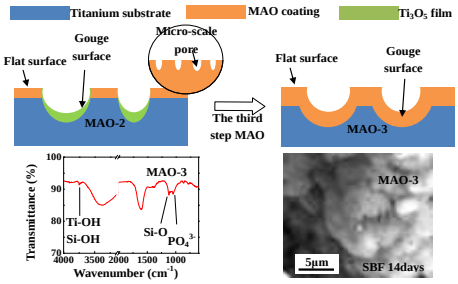

Development of conformal MAO coating on Ti plate with double-level porous surface, followed by characterization and evaluation in SBF.

Cite this: DOI: 10.1039/c0xx00000x

www.rsc.org/xxxxxx

ARTICLE TYPE

Conformal Coating Containing Ca, P, Si and Na with Double-level Porous Surface Structure on Titanium Formed by A Three-step Microarc Oxidation

Rui Zhou,[a] Daqing Wei,*[a] Jianyun Cao,[a] Wei Feng,[a] Su Cheng,[b] Qing Du,[a] Baoqiang Li,[a] Yaming Wang,[a] Dechang Jia[a] and Yu Zhou[a]

Received (in XXX, XXX) Xth XXXXXXXXX 20XX, Accepted Xth XXXXXXXXX 20XX
DOI: 10.1039/b000000x

A bioactive coating containing Ca, P, Si and Na elements with porous surface structure has been fabricated on titanium (Ti) plate by a three-step microarc oxidation. Randomly distributed gouges (80~200 μm) have been observed from the conformal MAO coating (with micro-scale pore size of 0.6~2μm in morphology) covered Ti surface which exhibits double-level porous structure. Meanwhile, it is noticed that Ca, P, Si and Na elements have been incorporated into the MAO coating but show different oxidation states of elements between the flat surface and gouge surface. The XPS results reveal that Ti-OH and SiO_2 gel have only formed on the gouge surface because of the declined microarc oxidizing ability in local area. Besides, the bioactivity of the different MAO steps prepared Ti plates has been examined by simulated body fluid (SBF) immersion. As expected, the three-step MAO prepared Ti with double-level porous surface structure exhibits the best apatite-inducing ability thanks to the as-introduced Ti-OH and Si-OH groups.

Introduction

Titanium (Ti) is attracting great attentions in the field of load bearing implant due to its extremely high mechanical properties, biocompatibility and bio-corrosive resistivity.[1] Unfortunately, Ti shows poor ossoeintegration property after implantation. Recently, it has been proved that the micro-scale pores in the size of 0.05~10 μm can promote the attachment and proliferation of osteoblast cells on Ti implants.[2-4] Meanwhile, the gouges in the size of 50~400 μm on implant surface can improve the fixation strength between implant and tissue after recovery by providing three-dimensional mechanical interlocking.[5-8] Therefore, several methods have been developed to fabricate topological structures on Ti surface, including sandblasting-acid etching,[9-11] anodic oxidation,[12] plasma spraying,[5,13] etc. However, the overwhelming majority of these materials do not show any bioactivity, owing to the lack of chemical stimulus to induce the apatite formation.[14] Once the unconnected interface becomes loose, the implants may normally fail to work or even be damaged. To address the drawbacks, microarc oxidation (MAO) has been used to modify the Ti surface, as both the incorporated elements and the topological structure of the MAO coating can be adjusted by changing the electrolyte compositions and process parameters.[15,16] Moreover, the formed MAO coating also exhibits excellent wear resistance ability,[17] which guarantees the long-term service of the MAO coated implant in the body. As a successful example, the sulfur and nitrogen incorporated MAO coatings with irregular grooves or gouges (5~20 μm in size) have been formed on Ti after treating in acidic electrolyte containing CH_3COOH or CH_3COONa,[18,19] which exhibit better bioactivity than the normally formed MAO coatings. However, it is still a great challenge to fabricate gouge with suitable size (80~200 μm) on Ti surface which shows the best shear strength between implant and bone after 12 weeks' recovery according to Bobyn's investigation.[20] Fortunately, the suitable gouges (80~200 μm) can be fabricated on MAO coated Ti surface via activating the corrosive ability of NO_3^- ions in electrolyte by changing the electrical parameters based on our previous work.[21] However, the micro-scale porous MAO coating is incomplete in the region of gouge surface due to the strong electrochemical corrosion during the second step MAO. Moreover, like the most of the MAO coating,[22-25] the two-step MAO prepared Ti plate shows poor apatite-inducing ability.[21] This phenomenon indicates that the effect of the MAO coating on the recovery of the bone in implantation site is very limited compared with those covered with bioactive film which show good apatite-inducing ability. Thus, method to improve the bioactivity of the MAO coating becomes a significant issue. Inspired by the relationship between functional groups and apatite-inducing ability, it is clear that Ti-OH and Si-OH groups are the key factors for the enhancement in apatite deposition,[26-28] but not the simply incorporated elements.[22-25,29] Herein, a third step MAO has been introduced into the procedure (Fig.1), as it will not only improve the integrity of the MAO coating by generating new coating on the gouge surface, but also can enhance elemental concentrations all over the porous surface film. Interestingly, we have observed that Ti-OH and SiO_2 gel have been introduced into the MAO coating on gouge surface after the third step MAO thanks to the previously Ti_3O_5 composed gouge surface film. Consistent with the previous investigations,[30-32] the as-introduced Ti-OH and Si-OH groups can effectively promote the apatite nucleation after SBF immersion, thus plays a dominant role in the enhancement of bioactivity. Understanding the effect of intermediate Ti_3O_5

film covered gouges, which formed during the second step MAO, on the third step MAO fabricated coating becomes a significant issue in the design and fabrication of OH groups introduced titanium oxide film on Ti surface.

In this work, we report the conformal coating containing Ca, P, Si and Na on Ti plate with double-level porous surface structure in micro and sub-millimetric scales, which is fabricated via three-step MAO. As expected, the three-step MAO prepared Ti plate exhibits good apatite-inducing ability due to the incorporation of Ti-OH and SiO_2 gel on the MAO coating covered gouge surface. Since there is no report about the MAO coating generated from Ti_3O_5 film covered gouges, its effects on the pore size distribution, phase composition, elemental concentration and oxidation states of the formed MAO coating are discussed thoroughly. Furthermore, thanks to the good bioactivity and potential mechanical interlocking effect provided by gouges, the three-step MAO prepared Ti is expected to be used as an advanced biomaterial in the aspect of medical implantation.

Experimental procedure

Materials preparation

Ti plates (30×30×1 mm^3) were ground with 200#, 600# and 1000# abrasive papers, washed by acetone and distilled water, then dried at 40 °C. In the MAO, three kinds of electrolytes were prepared for the different steps of MAO via dissolving of the reagent-grade chemicals into deionized water (listed in Table 1), and the pH value of the prepared electrolytes were 11.2, 13.3 and 13.2 corresponding to the MAO steps. Then, the as-prepared Ti plates were used as anodes, and stainless steel plate was used as cathodes in an electrolytic bath. The parameters for the different steps of MAO were listed in Table 2, and the schematic diagram for the procedure was shown in Fig.1. After the treatment, all the Ti plates that prepared after different steps of MAO were cut by wire electrical discharge machining into testing samples (10×10×1 mm^3). And then, ultrasonically washed by acetone and distilled water and dried at 40°C. In the following, these prepared Ti plates were labeled as MAO-1, MAO-2, and MAO-3 corresponding to the MAO steps.

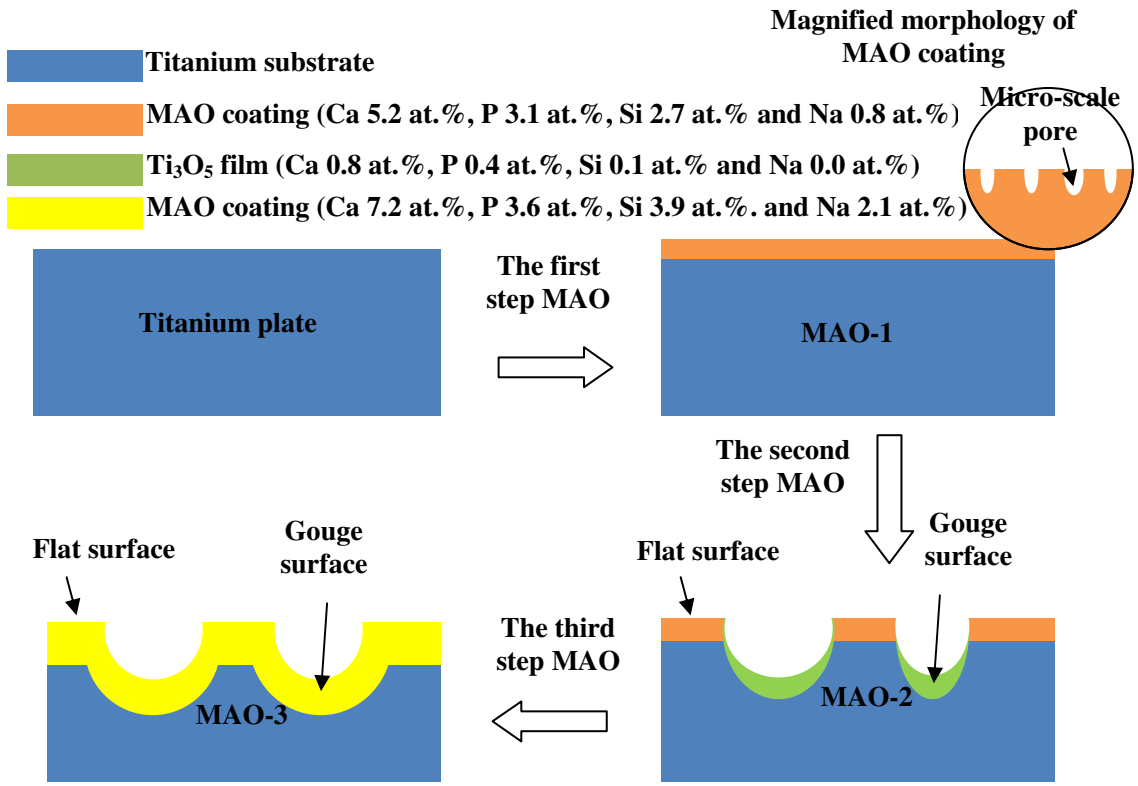

Fig.1 The schematic diagram for the procedure of the three-step MAO.

Table 1 Chemical concentration of the used electrolytes for different steps of MAO.

MAO step	Concentration ($g \cdot L^{-1}$)						PH
	EDTA-2Na	Na_2SiO_3	$Ca(CH_3COO)_2 \cdot H_2O$	$Ca(H_2PO_4)_2$	NaOH	$NaNO_3$	
1st	15	7.1	8.8	6.3	5	-	11.2
2nd	15	7.1	8.8	6.3	20	8.5	13.3
3rd	15	7.1	8.8	6.3	20	-	13.2

Cite this: DOI: 10.1039/c0xx00000x

www.rsc.org/xxxxxx

ARTICLE TYPE

Table 2 The parameters for the different steps of MAO

MAO step	Control Mode	Voltage (V)	Current (A)	Pulse Frequency (Hz)	Duty Cycle (%)	Oxidizing Time (min)
1st	Voltage constant	350	-	600	8	5
2nd	Current constant	-	8	600	8	5
3rd	Voltage constant	350	-	600	8	5

Simulated body fluid immersion

The MAO-1, MAO-2 and MAO-3 were soaked in 15 mL simulated body fluid (SBF) [33] for different time of 14, 21 and 28 days to examine their apatite-inducing ability. And the SBF was refreshed every other day. The SBF was prepared by dissolving reagent-grade chemicals of NaCl, $NaHCO_3$, KCl, $K_2HPO_4{\cdot}3H_2O$, $MgCl_2{\cdot}6H_2O$, $CaCl_2$, and Na_2SO_4 into deionized water. At last, it was buffered at pH 7.40 with tris-hydroxymethylaminomethane ($(CH_2OH)_3CNH_2$) and 1.0 mol·L^{-1} HCl at 37 °C.

Structure characterization

1 Raman spectrum. The surface compositions of the MAO-2 and MAO-3 were detected by laser Raman spectroscopy measurements (Raman, Jobin Yvon, France) with argon ion laser. The output power and wave were set at 20 mw and 458 nm, respectively.

2 Scanning electron microscopy (SEM) and energy dispersive X-ray spectrometer (EDS). Scanning electron microscopy (SEM, Helios Nanolab 600i, FEI Co., USA) was used to observe the surface morphology. Meanwhile, the elemental mapping images of the cross-section and the elemental concentrations of the samples were detected by an energy dispersive X-ray spectrometer (EDS, EDAX, USA) equipped on the SEM system. Additionally, the point EDS results with the detected regions of 1 μm^2 from the prepared sample surface (10×10×1 mm^3) were used for the surface chemical composition analysis.

3 X-ray photoelectron spectroscopy (XPS). An X-ray photoelectron spectroscopy (XPS, K-Alpha, Thermofisher Scienticfic Co., USA) was used to detect the chemical compositions of the MAO-1, MAO-2 and MAO-3. In the XPS experiment, an AlKα (1486.6 eV) X-ray source was used for the XPS work under a vacuum of 1.0×10^{-8} mbar. The current of X-ray beam was 6 mA and the resolution for energy was 0.5 eV with a scanning step of 0.1 eV. The regions of 400 μm^2 on the sample surfaces were analyzed. The measured binding energies were calibrated by the C1s (hydrocarbon C–C, C–H) of 285 eV. And the oxidation states of Ti, O, Si and P after Ar^+ ions etching for 60 s were analyzed.

4 Fourier transform infrared spectroscopy. Fourier transform infrared spectroscopy (FT-IR, Magna-IR 560 E.S.P., USA) was used to analyze the surface chemical structure of the MAO-3 before and after SBF immersion for 28 days. In the preparation, the powders were collected by blade scratching from the surface layer of the samples. Approximately 1 mg of the collected powder mixed with about 500 mg of dry KBr powder was ground using an agate mortar and pestle. The mixed powder was pressed into transparent disk with a diameter of 13 mm for the FT-IR work. In the FT-IR experiment, the scanning range and resolution were 4000~400 and 4 cm^{-1}, respectively. Additionally, at least 5 samples of the MAO-3 were used to collect enough powder by blade scratching, because the surface of MAO-3 was very hard.

5 X-ray diffraction (XRD). The surface phase compositions of the MAO-3 after SBF immersion for 28 days were analyzed by X-ray diffraction (XRD, D/max-γB, Japan) using a CuKα radiation with a continuous scanning mode at a rate of 4° min^{-1}. The accelerating voltage and current were set at 40 kV and 50 mA.

6 Mercury porosimetry. Mercury intrusion testing was used for analyzing pore size distribution and porosity of the MAO-1, MAO-2 and MAO-3, which was performed on vacuum dried samples using a mercury porosimetry (Micromeritics Autopore IV 9500 Instrument, Micrometrics, USA) at pressures up to 32 MPa.

7 Bonding strength test. The bonding strength between coating and substrate was investigated by the direct pull-off method. In pull-off tests, the sample (Φ30×1 mm^3) was bonded to the untreated steel using epoxy resin. The pull-off test was carried out on an electronic tensile testing machine (Instron1195, Instron Co., USA). A load to the coating was continually applied on the steel cylinder at a rate of 1.0 mm·min^{-1} until the sample was broken. The instant maximum load was recorded. The bonding strength was determined by Eq.1.

$$P = F_{max}/S \qquad \text{(Eq.1)}$$

Where F_{max} is the maximum load, S is the area of the coating surface, and P is the bonding strength.

Results

The surface photographs of the MAO-1, MAO-2 and MAO-3 are shown in Fig.2. Generally, the MAO steps directly lead to the change of surface morphology on the Ti plates. The MAO-1 exhibited a smooth surface as shown in Fig.2(a), while porous surface with gouges was observed on the MAO-2. It is interesting that the colour of gouges varied from black to white after the third step MAO (Fig.2(b) and (c)).

Cite this: DOI: 10.1039/c0xx00000x

www.rsc.org/xxxxxx

ARTICLE TYPE

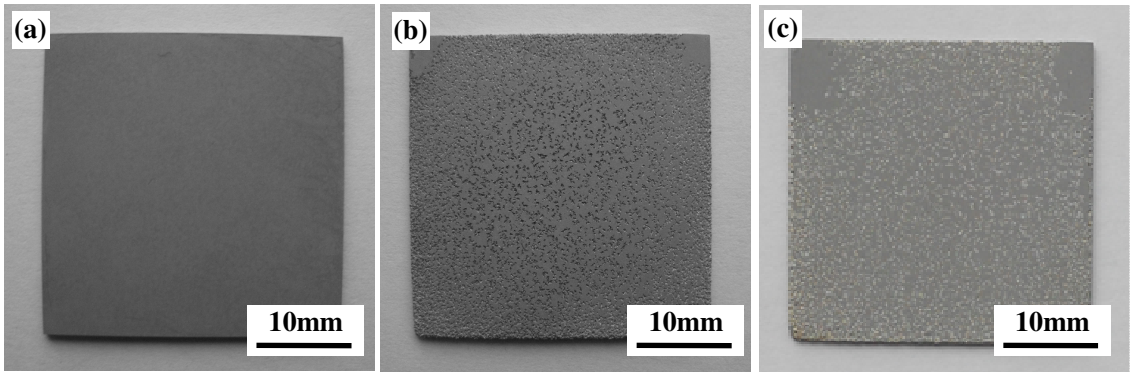

Fig.2 Surface morphologies of the (a) MAO-1, (b) MAO-2 and (c) MAO-3.

The SEM morphology revealed that the coating formed on the flat surface of the MAO-2 and MAO-3 (area B and D) exhibited rough and micro-scale porous structure (0.6~2 μm in diameter), which was similar with that formed on the MAO-1 surface (Fig.3(a), (d) and (f)). Meanwhile, the MAO coating was incomplete in the gouge surface of the MAO-2 (area C). Besides, the gouge surface was covered with a dense oxide film (Ti 32.1 at.%, O 63.5 at.%), which did not show any micro-scale pore. In the case of the MAO-3, the micro-scale porous coating was conformally formed on the whole surface as expected, but the micro-scale pore size in the deep gouge surface was smaller than that formed on the flat surface (Fig.3(f) and (g)).

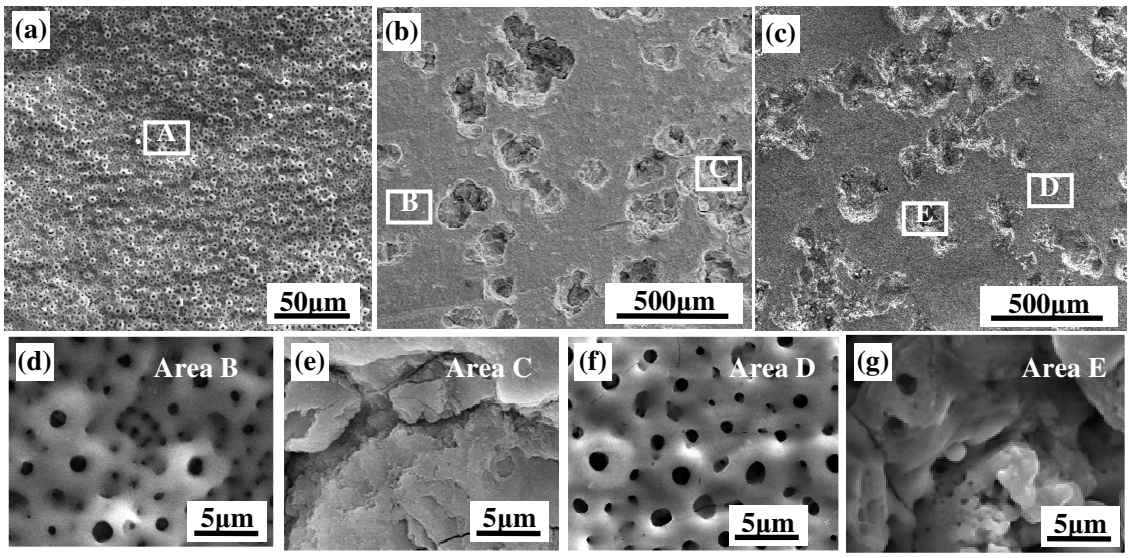

Fig.3 SEM morphology of the (a) MAO-1, (b) MAO-2 and (c) MAO-3. Additionally, the regions with different features were also observed: (d) magnified morphology of area B, (e) magnified morphology of area C, (f) magnified morphology of area D, and (g) magnified morphology of area E.

Fig.4 shows the mercury intrusion analysis of the MAO-1, MAO-2 and MAO-3, from which obvious differences in pore size distribution and porosity were observed. The pore size distribution curve of the MAO-1 showed unimodal distribution feature, the pore size was mainly located at 20~30 μm. However, those of the MAO-2 and MAO-3 exhibited double-peaks distribution, the two peak distribution ranges were 20~30 μm and 80~200 μm, respectively. In contrast, the intensity of the peak located at the range of 20~30 μm for the MAO-3 was strongly enhanced. The difference in pore size distribution between the SEM morphology and mercury intrusion analysis would be attributed to the structure of the formed micro-scale pores, which is normally considered as discharge channel. Due to the discharge channel (micro-scale pore) directly connects the electrolyte with Ti substrate,[34] the size of the cavity for the micro-scale pore is larger than that observed from the surface SEM morphology. As shown in Fig.4(b), the porosity of the Ti plates after different steps of MAO increased steadily from 1.78% (MAO-1) to 4.23%

(MAO-3), which is consistent with the pore size distribution result.

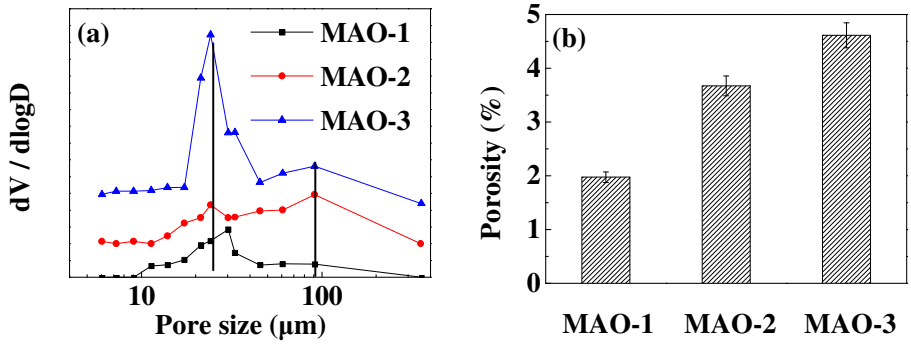

Fig.4 Mercury intrusion analysis of the Ti plates after different steps of MAO: (a) pore size distribution for the Ti plates after different steps of MAO determined by Hg porosimetry and (b) porosity of the Ti plates after different steps of MAO.

Fig.5 shows the cross-sectional morphology of the MAO-1, MAO-2 and MAO-3. Obviously, the strong electrochemical corrosion during the second step MAO not only corroded gouges on the MAO covered Ti surface, but also generated a dense titanium oxide film on the surface of gouges. As-expected, a micro-scale porous and integral MAO coating was observed from the cross-sectional morphology of the MAO-3 in Fig.5(c). Besides, the thickness of the coating steadily increased from 3.9 μm (MAO-1) to 12.3 μm (MAO-3) after the next two steps MAO. Additionally, it was also noticed that the depth of the corroded gouges was about 70 μm.

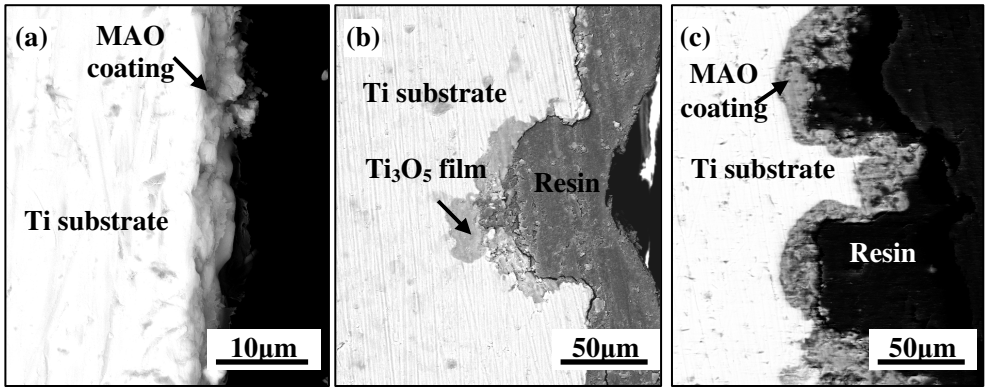

Fig.5 Cross-sectional morphology of the (a) MAO-1, (b) MAO-2, and (c) MAO-3.

Fig.6 shows SEM cross-sectional image and EDS mapping images of the MAO-3. The result confirmed that Ca, P, Si and Na had been incorporated into the MAO coating, no obvious difference was observed between flat surface and gouge surface. Whereas, the EDS point results also revealed that the concentration of Ca (6.5 at.%), P (3.2 at.%) and Si (3.7 at.%) in the gouge surface was a little bit less than that deposited on the flat surface (Ca 7.4 at.%, P 3.6 at.% and Si 4.1 at.%), attributing to the increased specific surface area which dispersed the microarc oxidizing intensity. Additionally, the uniformly presentation of Si on the cross-sectional image of the MAO-3 should be attributed to the randomly inlaid SiC particles during the grinding process.

Cite this: DOI: 10.1039/c0xx00000x

www.rsc.org/xxxxxx

ARTICLE TYPE

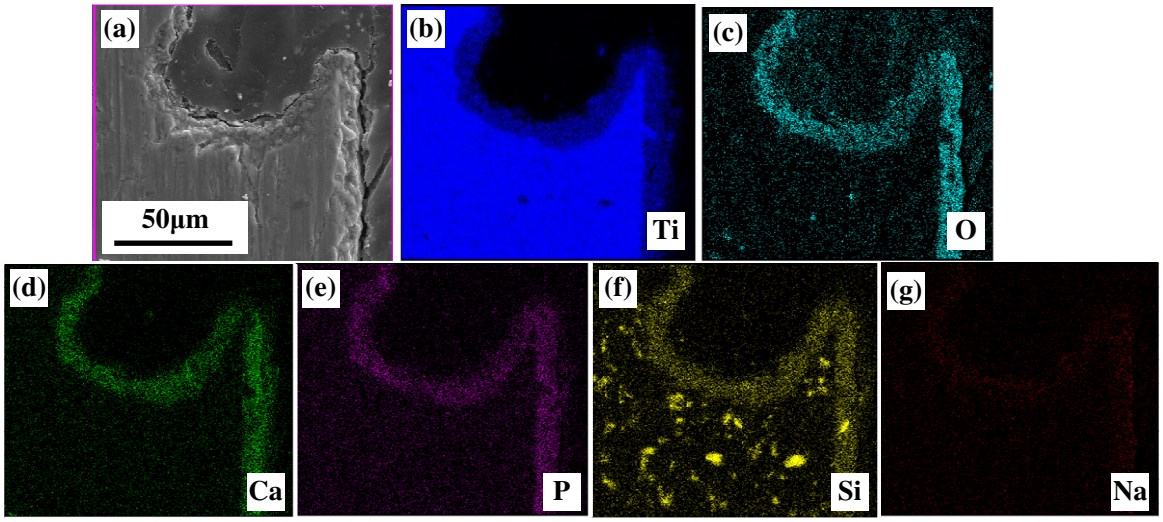

Fig.6 The image and EDS mapping images of the cross-sectional morphology of the MAO-3: (a) SEM morphology, (b) Ti, (c) O, (d) Ca, (e) P, (f) Si and (g)Na.

Fig.7 shows the Raman spectra which are detected from different regions of the MAO-2 and MAO-3, namely, flat surface (corresponding to area B and D in Fig.3) and gouge surface (corresponding to area C and E in Fig.3). As consistent with our previous study, [21] the characteristic peaks of anatase [35,36] at 148, 396, 512 and 641 cm^{-1} were identified from the spectra of the coating formed on the flat surface of the MAO-2 and MAO-3 (Fig.7(a) and (b)). Though different MAO control modes were conducted on sample during the second step MAO, the characteristic peaks of Ti_3O_5 were also detected from the gouge surface of the MAO-2, including symmetric stretching vibration of O-Ti-O at 155 cm^{-1}, symmetric bending vibration of O-Ti-O at 420 cm^{-1}, and function of symmetric stretching and bending vibration at 607 cm^{-1} (Fig.7(c)).[21,35] Interestingly, the gouge surface of the MAO-3 with rough and micro-scale porous structure would be consisted by both anatase and Ti_3O_5, as the spectrum is superposed by the characteristic peaks of the curve (b) and (c) in Fig.7.

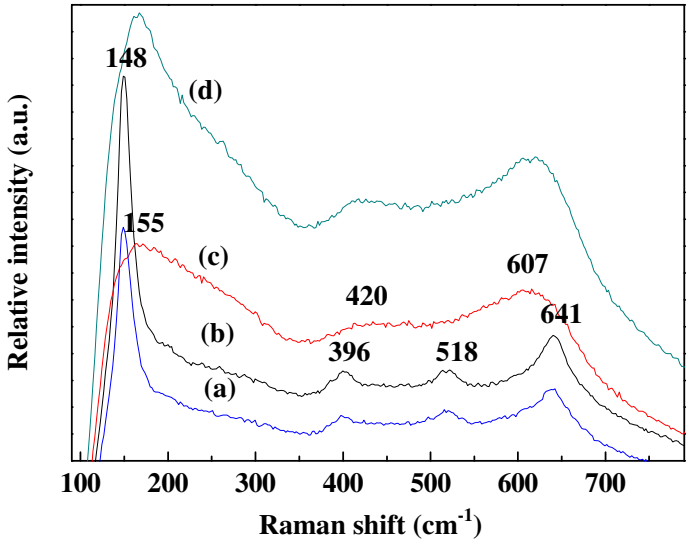

Fig.7 The Raman spectra of the MAO-2 and MAO-3 detected from different feature regions: (a) flat surface of the MAO-2, (b) flat surface of the MAO-3, (c) gouge surface of the MAO-2, and (d) gouge surface of the MAO-3.

Cite this: DOI: 10.1039/c0xx00000x

www.rsc.org/xxxxxx

ARTICLE TYPE

In order to determine the surface element composition and oxidation states of the synthesized layers, XPS was detected from both flat surface and gouge surface on Ti plates prepared after different steps of MAO. As shown in Fig.8, the detected elements primarily consist of Ti and O, and traces of Ca, P, Si, Na and C are also observed. Furthermore, only a small amount of N has been incorporated into the MAO-2 and MAO-3 surfaces. Additionally, the high-resolution XPS spectra reveal that there are obvious differences in oxidation states (of Ti 2p, O 1s, P 2p and Si 2p) between flat surface and gouge surface, while the oxidation states of the synthesized layers in the flat surface remain steadily after different steps of MAO (Fig.9 and 10).

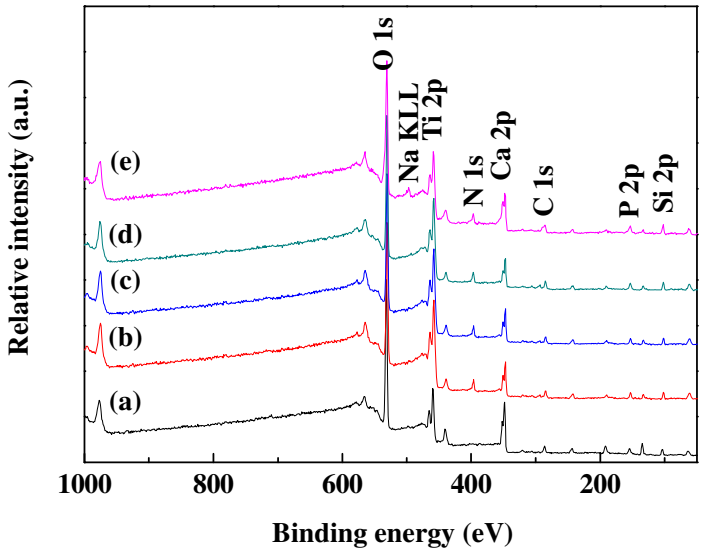

Fig.8 The XPS survey of the MAO-1, MAO-2 and MAO-3 detected from different feature regions: (a) flat surface of the MAO-1, (b) flat surface of the MAO-2, (c) flat surface of the MAO-3, (d) gouge surface of the MAO-2, and (e) gouge surface of the MAO-3.

Fig.9 shows the high-resolution XPS spectra of P 2p and Si 2p. The P 2p peaks of the coating surfaces were well fitted at 133.3 eV, which was assigned to P 2p in PO_4^{3-} (at 133.4 eV), but small amount of HPO_4^{2-} (at 134.4 eV) was detected from the gouge surface of the MAO-3.[37] In the case of Si 2p, the binding energy at 102.4 eV corresponding to Si^{4+} (Si-O) was observed from all the Si 2p spectra of samples.[38] However, new binding energy at 104.2 eV was also detected from the gouge surface of the MAO-3, pointing to the formation of SiO_2 gel.[39]

Cite this: DOI: 10.1039/c0xx00000x

www.rsc.org/xxxxxx

ARTICLE TYPE

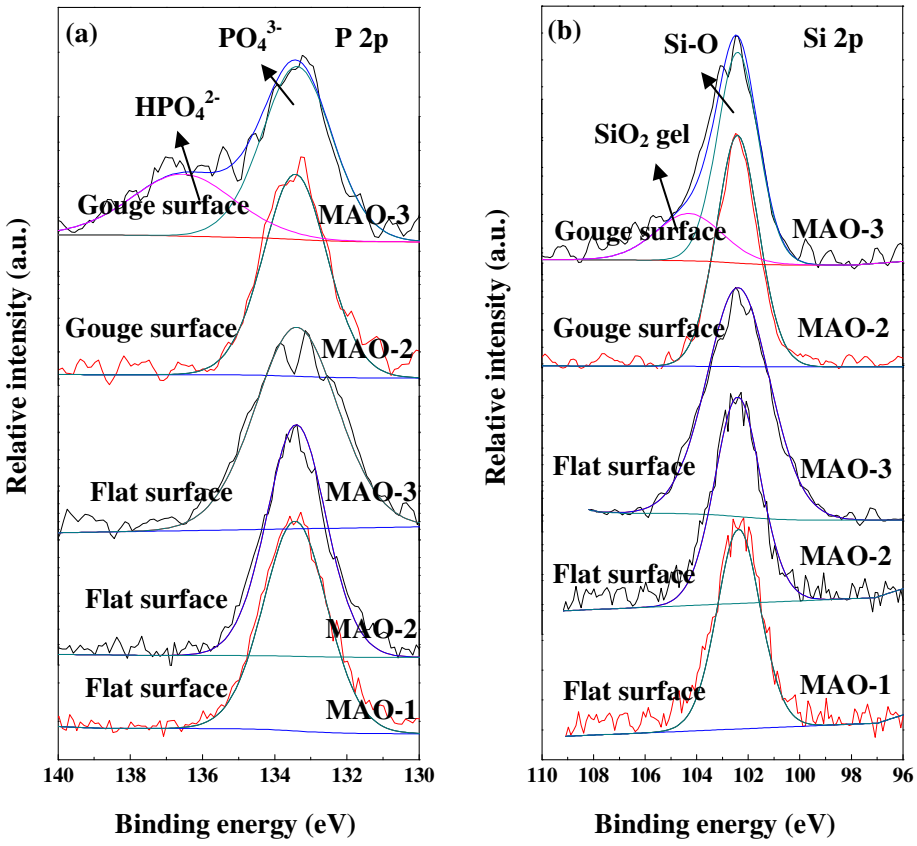

Fig.9 The high-resolution XPS spectra of P2p and Si2p detected from the MAO-1, MAO-2 and MAO-3: (a) P2p, (b) Si2p.

Deconvolution of the Ti 2p peak revealed that the titanium mainly existed as Ti^{4+} (TiO_2 anatase) on the flat surface, but another peak of Ti 3/2p at 457.4 eV corresponding to Ti^{2+} appeared in the gouge surface of the MAO-2 and MAO-3 (Fig.10).[40] Furthermore, the relative area ratio of the peaks fitting results indicated that the atomic ratio of Ti^{4+} / Ti^{2+} in the gouge surface of the MAO-2 was about 2:1, while it varied to 4:1 in the gouge surface of the MAO-3. This reveals that some titanium oxide with low oxidation state in Ti element remains in the gouge surface after the third step MAO, which is consistent with the Raman spectra results (Fig.7(d)).

According to the literatures,[38,41-46] the original O 1s spectra of all the flat surfaces were assigned to TiO_2 (anatase) (at 530.1 eV).[38,41-44] Whereas, a second peak at 531.8 eV corresponding to O1s in titanium oxide with lower Ti oxidation state (like TiO) was obtained from gouge surfaces of the MAO-2 and MAO-3.[38] Associated with the Raman results (Fig.7) and the atomic ratio of Ti^{4+} / Ti^{2+}, the phase of this titanium oxide was identified as Ti_3O_5. Additionally, a third peak of O1s at 532.8 eV was also detected from the gouge surface of the MAO-3, indicating the incorporation of basic hydroxyl and physical bound water after the third step MAO.[43,46]

Cite this: DOI: 10.1039/c0xx00000x

www.rsc.org/xxxxxx

ARTICLE TYPE

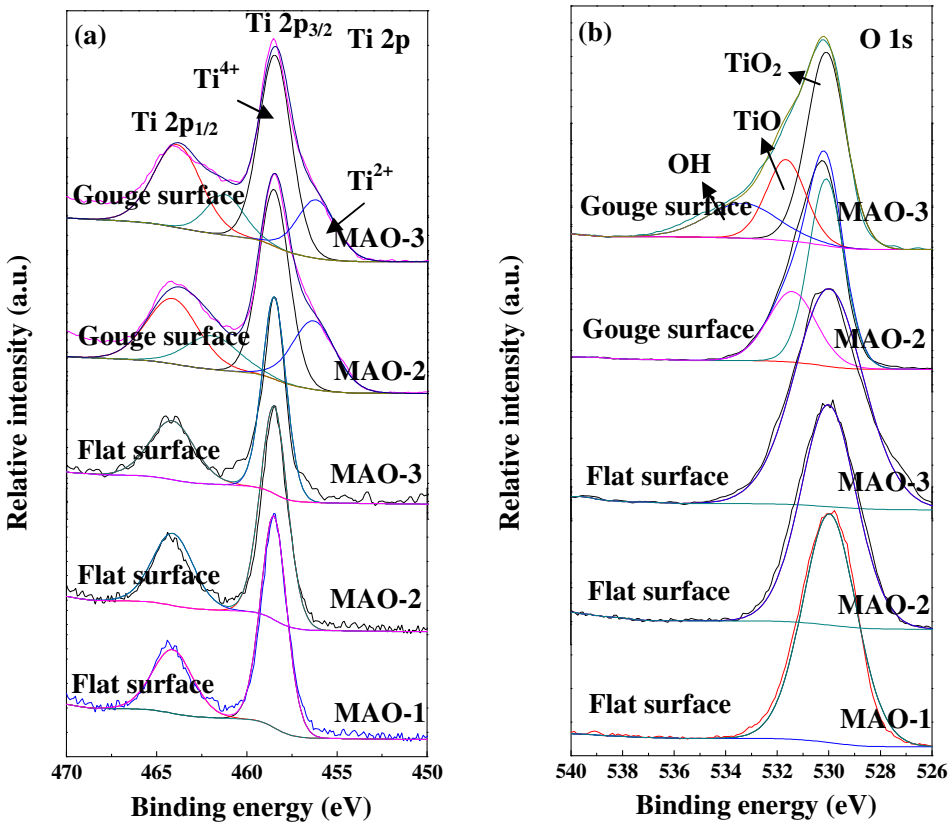

Fig.10 The high-resolution XPS spectra of O1s and Ti2p detected from the MAO-1, MAO-2 and MAO-3: (a) Ti2p, (b) O1s.

As shown in Fig.11, OH^- absorption band at 1650 and 3380 cm^{-1},[46] and Si-O absorption band [47] at 1130 cm^{-1} were observed from the FT-IR spectrum of the MAO-3 surface. Meanwhile, Ti-OH and Si-OH absorption band at 3750 cm^{-1} was also detected,[28,48] which was consistent with the formation of the basic OH group in Ti-OH and SiO_2 gel on the gouge surface of the MAO-3 (Fig.9 and 10). In addition, PO_4^{3-} absorption band at 1033 cm^{-1} was also detected by FT-IR spectrum.[49]

Cite this: DOI: 10.1039/c0xx00000x

www.rsc.org/xxxxxx

ARTICLE TYPE

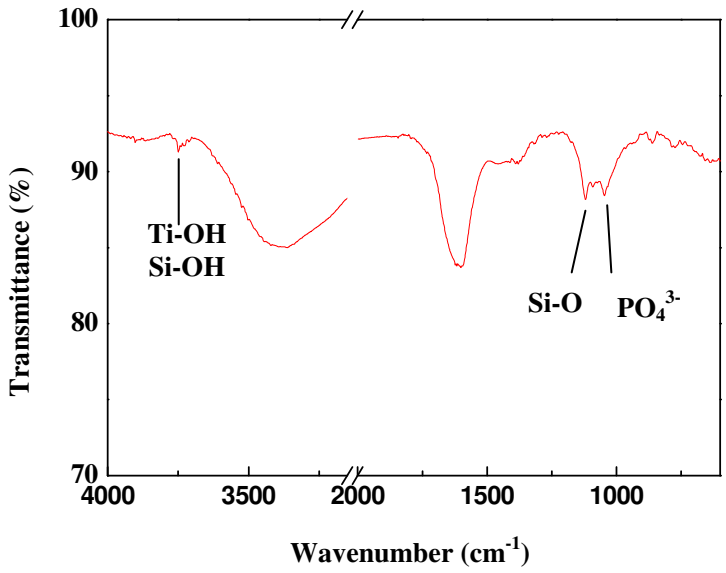

Fig.11 FT-IR spectrum of the MAO-3 surface.

Fig.12(a) shows the bonding strength of the coatings formed on the MAO-1, MAO-2 and MAO-3. According to the calculated results, the bonding strength for the Ti plates after different steps of MAO increased steadily from 20.1 ± 3.1 MPa to 28.2 ± 3.4 MPa. The fracture morphologies reveal that the MAO coating on the MAO-2 was almost wholly peeled off from the substrate, its measured bonding strength should be identified as adhesive strength (Fig.12(b)). However, in the case of the MAO-1 and MAO-3, the surface coatings were only partly peeled off from the substrates (Fig.12(b)). Thus, the bonding strength should be considered as the fracture strength. Meanwhile, the adhesive strength of these two samples with ideal structure (none crack and defect) should be higher than the measured one. Besides, it was also noticed that the SEM residual epoxy resin (C 83.3 at.% and O 15.1at.%) was also observed from the gouges on the MAO-2 and MAO-3 (Fig.12(c) and (d)), which provides three-dimensional mechanical interlocking for improving the bonding strength. This would be the reason why the coating of MAO-2 with incomplete MAO coating exhibited higher bonding strength than that of the MAO-1.

Cite this: DOI: 10.1039/c0xx00000x

www.rsc.org/xxxxxx

ARTICLE TYPE

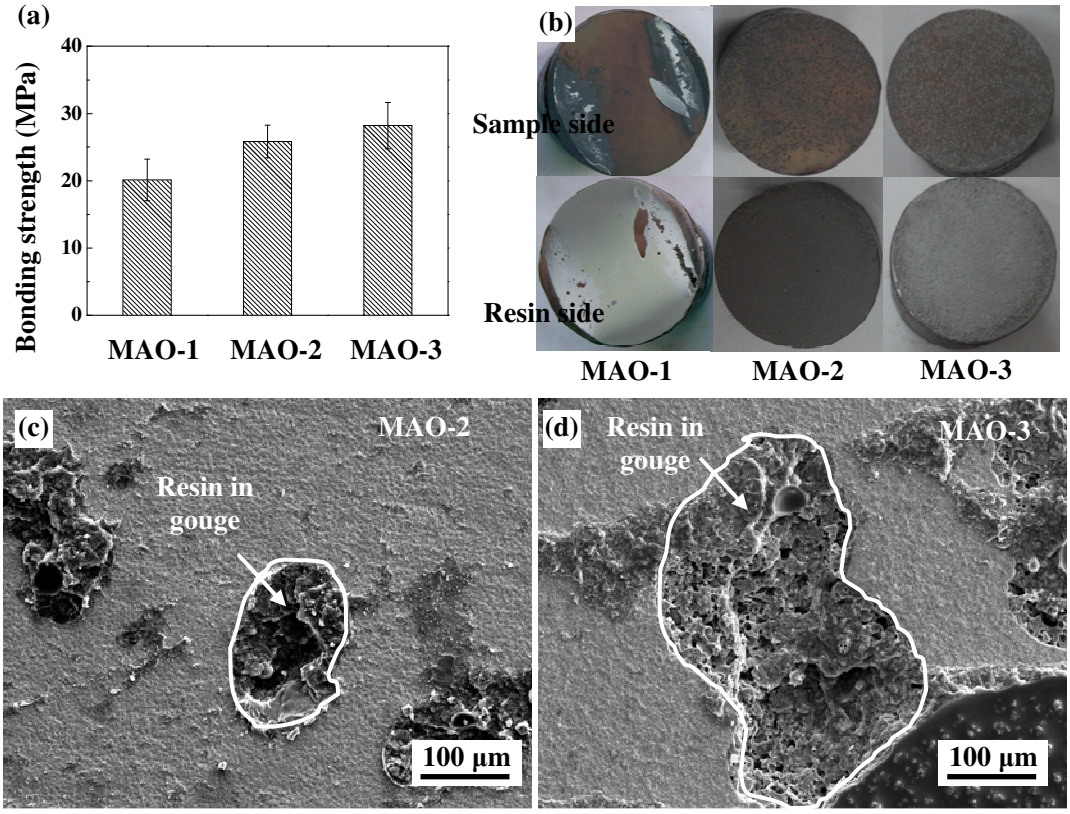

Fig.12 Bonding strength and fracture morphologies of the coatings formed on the MAO-1, MAO-2 and MAO-3: (a) boding strength of the coatings, (b) fracture morphologies of the MAO-1, MAO-2 and MAO-3, (c) SEM morphology of the fracture surface on the MAO-2, and (d) SEM morphology of the fracture surface on the MAO-3.

Fig.13 shows the SEM morphology of the MAO-1, MAO-2 and MAO-3 surfaces after SBF immersion for different time. After SBF immersion for 14 days, no apatite was found on the surfaces of the MAO-1 and MAO-2 (Fig.13(a) and (b)). However, it was observed that the net-work film which was mainly consisted by Ca (23.9 at.%), P (12.8 at.%) and O (54.3 at.%) was deposited on the gouge surface of the MAO-3 (Fig.13(c) and (j)). These results indicate the apatite-inducing ability of the MAO-3 surface is significantly higher than that of the MAO-1 and MAO-2. After SBF immersion for 21 days, there was still no change on the MAO-1 surface (Fig.13(d)), while deposit nuclei was observed from the gouge surface of the MAO-2 (Fig.13(e) and (k)). Besides, the gouge of the MAO-3 was almost filled up by the Ca and P enriched deposits (Fig.13(f)). Further increasing the immersion time to 28 days, the Ca and P enriched deposits were observed from all the samples (Fig.13(g), (h) and (i)). Same, the apatite-inducing ability of the MAO-3 surface is better than those of the MAO-1 and MAO-2 yet, since the whole surface of the MAO-3 is covered by the deposits film.

Cite this: DOI: 10.1039/c0xx00000x

www.rsc.org/xxxxxx

ARTICLE TYPE

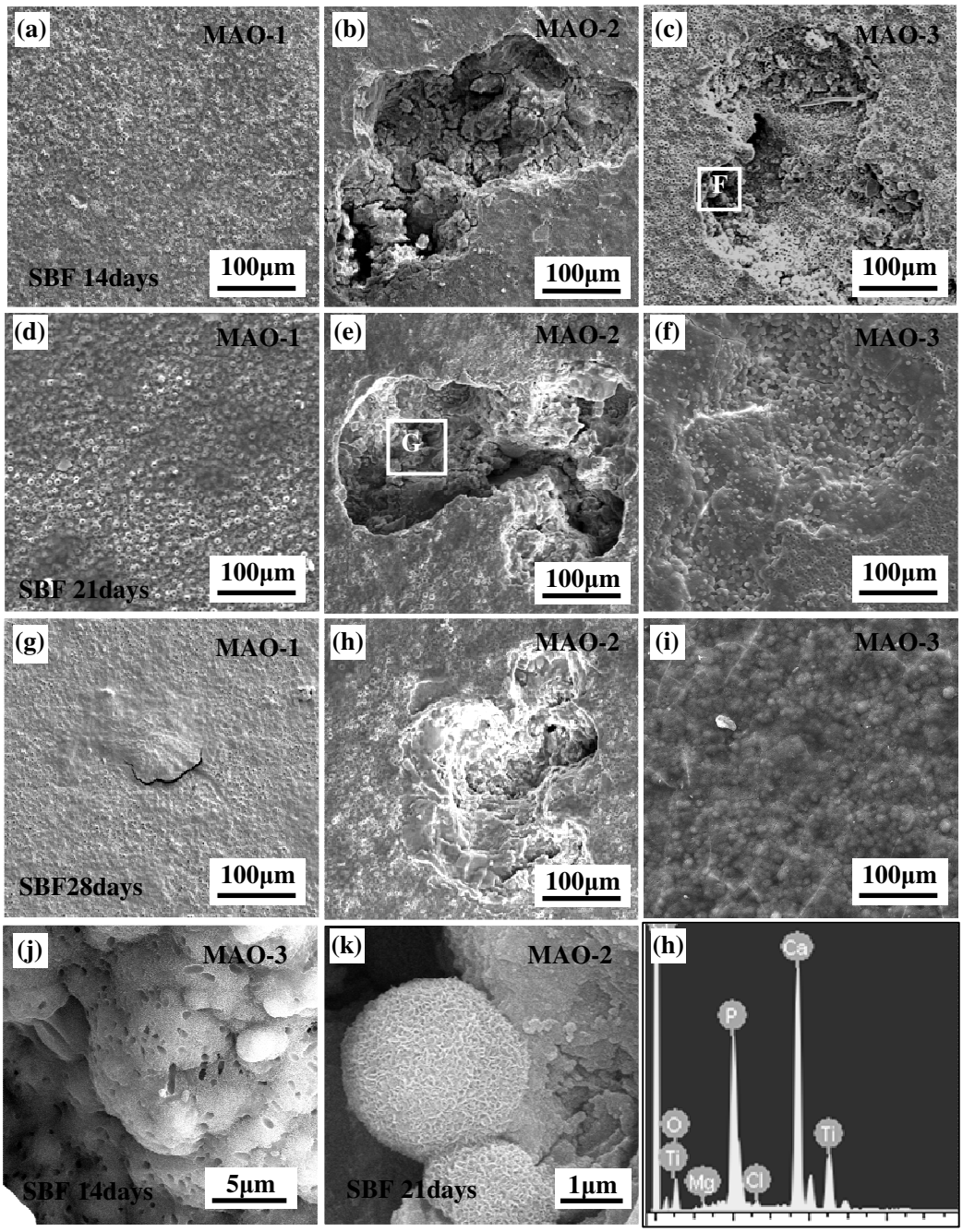

Fig.13 SEM morphologies of the MAO-1, MAO-2 and MAO-3 after SBF immersion for different time: (a), (b) and (c) MAO-1, MAO-2 and MAO-3 for 14 days; (d), (e) and (f) MAO-1, MAO-2 and MAO-3 for 21 days; (g), (h) and (i) MAO-1, MAO-2 and MAO-3 for 28 days; (j) the magnified morphology of area F, (k) magnified morphology of area G in Fig.13(c) and (h) EDS spectrum of area G in Fig.13(e).

Fig.14 shows the XRD patterns of the MAO-3 after SBF immersion for 28 days. Obviously, the diffraction peaks of apatite at 26.3° and 32.5° were detected, confirming that the MAO-3 surface had apatite-inducing ability.

Cite this: DOI: 10.1039/c0xx00000x

www.rsc.org/xxxxxx

ARTICLE TYPE

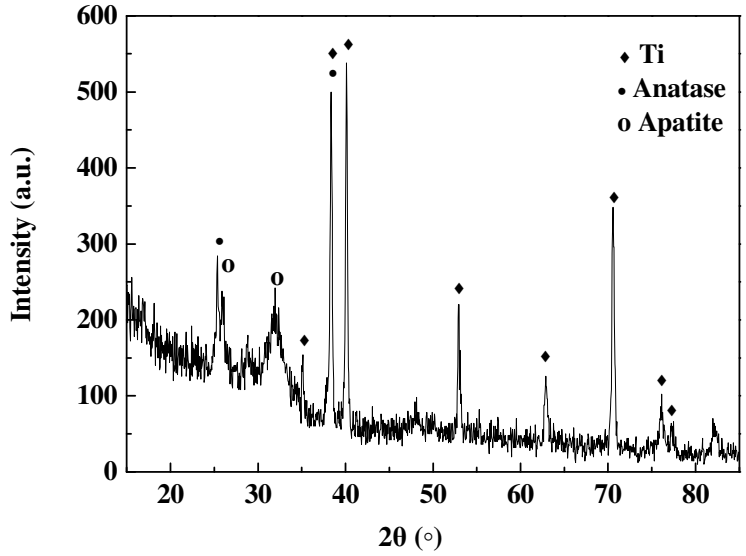

Fig.14 XRD pattern of the MAO-3 after SBF immersion for 28 days.

Fig.15 shows the FT-IR spectrum of the MAO-3 surface after SBF immersion for 28 days. OH^- absorption bands at 1651 and 3470 cm^{-1}, PO_4^{3-} absorption bands at 1033, 602 and 566 cm^{-1}, as well as CO_3^{2-} absorption bands at 1462, 1421, and 872 cm^{-1} were observed from the FT-IR spectrum.[49] Besides, the HPO_4^{2-} groups were detected with the characteristic peaks of 1099, 956 and 874 cm^{-1}.[49] All these results confirmed that the apatite with carbonated structure was formed on the MAO-3 surface.

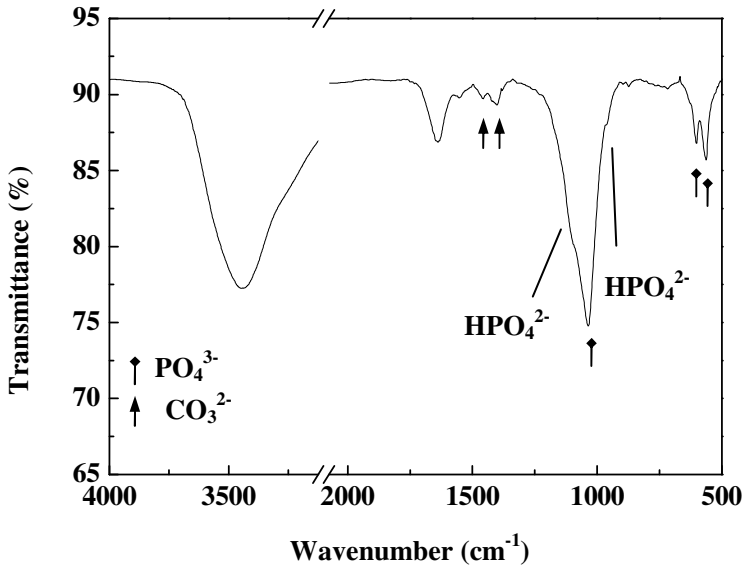

Fig.15 FT-IR spectrum of the MAO-3 surface after SBF immersion for 28 days.

Cite this: DOI: 10.1039/c0xx00000x

www.rsc.org/xxxxxx

ARTICLE TYPE

Discussion

The effect of Ti_3O_5 film in gouge surface on the formation of MAO coating

After the third-step MAO, randomly distributed gouges (80~200 μm) covered by conformal MAO coating (with micro-scale pore size of 0.6~2μm in morphology) on Ti plate surface have been achieved, which exhibits a unique double-level porous structure. However, obvious differences in surface morphology, phase composition, elemental concentration and oxidation states are also observed between the MAO coatings formed on the gouge surface and flat surface. These phenomena are quite different from the uniform MAO coating reported by Xie and Liu,[18,19,50] as well as the microarc oxidized porous Ti substrate (formed by sintering titanium beads) proposed in our previous study.[51] The reason for this result would be attributed to the difference in substrate between gouge surface and flat surface on the MAO-2, since it is the only difference between the previous work and this investigation, besides the surface topological structure. Namely, the characteristics of the formed MAO coating are not obviously influenced by the surface topological structure, but dominated by the substrate materials.

According to the SEM and Raman results, it is clear that the as-used MAO-2 for the third step MAO is covered by the rough and micro-scale porous MAO coating on the flat surface, but dense Ti_3O_5 film in the gouge surface (without any micro-scale pore).

In the case of flat surface, as the micro-scale porous structure has provided the discharge plasma channel which is directly connected with titanium substrate, the microarc oxidizing reaction always occurs at the interface between the already formed MAO coating and Ti substrate.[52] Consistent with this view, no obvious difference is observed from the flat surface of the MAO-1, MAO-2 and MAO-3, but the increase in coating thickness due to the prolongation of treating time.

To the item of gouge surface, the size of the formed micro-scale pores on the MAO-3 is smaller than that formed on the flat surface, indicating the decline of microarc oxidizing ability in this region during the third step MAO. This would be attributed to the high stability of titanium oxide compared with pure Ti.[53] It is clear that Ti_3O_5 (26492-ICSD) has the familiar basic atomic unit structure (TiO_6 octahedral) with anatase (Fig.16), but shows a little bit difference in bond length due to the orbital hybridization of the titanium atoms with lower state (Ti^{2+} according to Fig.10). Therefore, the dense Ti_3O_5 film is hard to be corroded or further oxidized, as the reconstruction of the stable lattice structure needs to consume large amounts of energy. Furthermore, though the phase transformations of Ti and Ti_3O_5 to anatase are spontaneous reactions (Eq.2 and 3), the oxidation of Ti_3O_5 to anatase still needs to consume more energy for the instantly completion during third step MAO compared with Ti substrate due to the high ΔG^{θ} value. Moreover, the increased specific surface area in gouge area further disperses the insufficient discharge energy. As a result, the MAO coating is hard to be formed on the previously Ti_3O_5 composed gouge surface during the third step MAO, showing small microarc oxidized pore size. Once the micro-scale pores, which are normally considered as the discharge plasma channel, are successfully connected with the substrate, new MAO coating is generating based on the Ti substrate but not the Ti_3O_5 film. Additionally, the Raman and XPS results (Fig.7 and 10) reveal that some of Ti_3O_5 phase has remained in the gouge surface after the third step MAO, which strongly support our point.

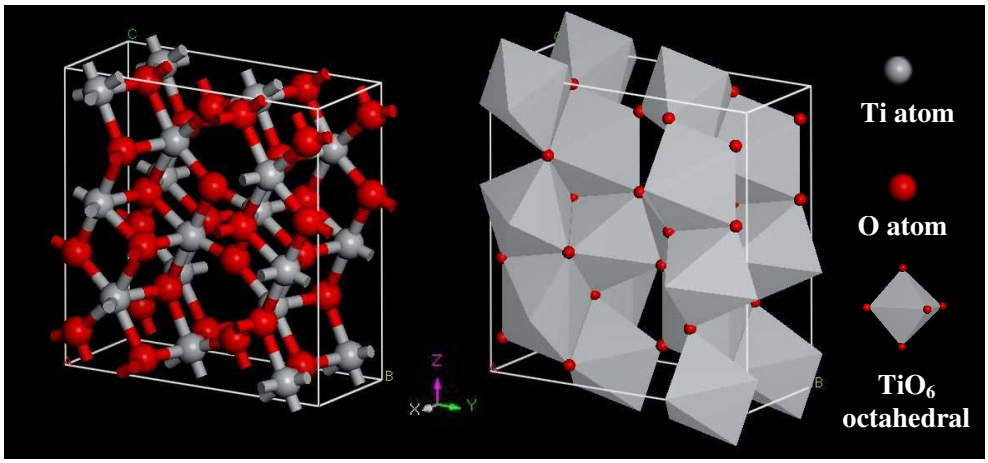

Fig.16 Schematic diagram for the atomic structure of Ti_3O_5 (26492-ICSD).

$$Ti(s)+2H_2O(l)=TiO_2(s)+2H_2(g) \quad \text{(Eq.2)}$$

($\Delta G^{\theta}(298K)= -414.5$ KJ·mol^{-1}, $\Delta H^{\theta}= -372.4$ KJ·mol^{-1}, $\Delta S^{\theta}= 141.3$ J·mol^{-1}·K^{-1})

$$Ti_3O_5(s)+H_2O(l)=3TiO_2(s)+H_2(g) \quad (Eq.3)$$

($\Delta G^{\theta}(298K)= -111.6$ KJ·mol^{-1}, $\Delta H^{\theta} = -86.8$ KJ·mol^{-1}, $\Delta S^{\theta} = 83.2$ J·mol^{-1}·K^{-1})

At the same time, it is also noticed that the Ti-OH and SiO_2 gel are also introduced into the gouge surface after the third step MAO (Fig.11), which are not observed in Liu and Xie's investigations as well as our previous studies.[18,19,50,51] Since the only change in the gouge surface is the formed Ti_3O_5 film after the second step MAO, it should be considered as the dominant factor. Based on the above discussion, this phenomenon can be explained as the decline of the microarc oxidizing ability in the gouge surface during the third step MAO, which is directly caused by the relatively electrochemical stable Ti_3O_5 film. Namely, due to the reduction in the provided discharge energy based on per unit surface area, the deposited ions in the gouge surface can not be treated as those in the flat surface, which are fully oxidized and incorporated into the MAO film as amorphous phase.[54] Thus, the deposited hydrate compounds are fortuitously existed as the silica gel and Ti-OH on the gouge surface due to the incomplete oxidation with relatively low oxidizing intensity (Fig.9,10 and 11).

Apatite-inducing ability

The SBF immersion experiments demonstrate that apatite can be induced on the surface of the MAO-1, MAO-2 as well as MAO-3, and the time for apatite induction on the MAO-3 was significantly shortened compared to that on the MAO-1 and MAO-2. Based on the SBF immersion results, it is speculated that the induction of apatite is closely related to the gouges, particularly the oxidation states of Ti and Si in the MAO coatings.

However, the MAO-1 surface had no such gouges but still induced apatite after SBF immersion for 28 days. The reason for apatite induction on the MAO-1 is possibly due to the incorporated elements. According to the results proposed by Song and et al,[24] the incorporated Ca and P ions in the MAO coating are hydrolyzed to yield Ca^{2+}, OH^-, and HPO_4^{2-} ionic species possibly generating a Ti-OH on surface. Meanwhile, the previous works also indicates that the hydrated silica gel layer is possible to form on the Ca, P, Si and Na incorporated MAO coating surface during the SBF immersion as listed in Eq.4.[26,36]

$$Si(OSi)_3ONa+H_2O \rightarrow Si(OSi)_3OH+Na^+ +OH^- \quad (Eq.4)$$

The Ti-OH and Si-OH groups increase the local degree of supersaturation with respect to apatite near the surface. When the apatite nuclei are formed, they spontaneously grow at the expense of calcium and phosphate ions from the SBF solution. Thus, the apatite has been induced on the MAO-1 surface, but it needs a long time (28 days) for the ions exchange process.

In the case of MAO-2, the corroded gouges which significantly increase the specific area in the gouge area can trigger the formation of more hydrated silica gel and Ti-OH on surface.[21] This promotes an increase in the local degree of supersaturation with respect to apatite near the surface which triggers apatite nucleation. Therefore, the gouge surface of MAO-2 shows shorter time for apatite induction than that of the MAO-1 surface.

As to the item of MAO-3, it shows similar surface structure (gouge) with that of the MAO-2, but the time for apatite induction on the MAO-3 has been significantly shortened. This is attributed to the functional groups in the gouge surface. According to the XPS and FT-IR results (Fig.9, 10 and 11), the Ti-OH and silica gel layer have formed on the gouge surface of the MAO-3 after the third step MAO. These already formed surface hydroxyl groups (Si-OH and Ti-OH) are known to be efficient inducers of apatite nucleation,[33,35–40,53] which dramatically reduces the SBF immersion time for apatite nucleation via ions exchange of Ca, P and Na. As a result, a network like apatite film has been formed on the gouge surface of the MAO-3 after less than 14 days.

Therefore, we propose that the gouge which increases the specific area of the MAO coated Ti plate can promote apatite induction, but the formed Ti-OH and Si-OH is the dominant factor for the enhanced apatite-inducing ability. As a result, the MAO-3 which exhibits both the suitable gouge size and the best apatite-inducing ability for achieving excellent shear strength between implant and bone is expected to be used as an advanced biomaterial in the aspect of medical implantation.

Conclusions

Conformal coating covered Ti plate with double-level porous surface structure has been fabricated via a three-step microarc oxidation. The elements of Ca, P, Si and Na have been successfully incorporated into the MAO coating with conformal micro-scale porous structure in both the gouges surface and flat surface. Since the dense Ti_3O_5 film with high stability has previously formed in the gouge surface after the second step MAO, the formation of MAO coating in this region becomes difficult compared with that on flat surface. Meanwhile, hydrate compounds are fortuitously existed as the silica gel and Ti-OH on the gouge surface due to the incomplete microarc oxidation with relatively low oxidizing intensity. As a result, the three-step MAO prepared Ti plate exhibits good apatite-inducing ability, attributing to the as-introduced Si-OH and Ti-OH group which is the dominant factor for triggering apatite nucleation.

Acknowledgements

This work was financially supported by National Basic Science Research Program (2012CB933900), National Natural Science Foundation of China (Grant No. 51321061, 51002039 and 51021002), Youth Science Fund Project in Heilongjiang Province (QC2013C043), Fundamental Research Funds for the Central Universities (Grant No.HIT.NSRIF.2014002), and National Scholarship for Postgraduate student.

Notes and references

[a] *Department of Materials Science and Engineering, Harbin Institute of Technology, Harbin, P.R. China. Fax: +86-451-8641-4291; Tel: +86-451-8640-2040-8403; E-mail: daqingwei@hit.edu.cn*

[b] *School of Architecture and Civil Engineering, Harbin University of Science and Technology, Harbin, P.R. China.*

1 M. Geetha, A. K. Singh, R. Asokamani and A. K. Gogia, *Prog. Mater. Sci.*, 2009, **54,** 397.

2 K. D. Yun, Y. Yang, H. P. Lim, G. J. Oh, J. T. Koh, I. H. Bae, J. Kim, K. M. Lee and S. W. Park, *Mater. Sci. Eng. C*, 2010, **30**, 27.

3 R. A. Gittens and T. McLachlan, *Biomaterials*, 2011, **32**, 3395.

4 A. L. Raines and R. Olivares-Navarrete, *Biomaterials*, 2010, **31**, 4909.
5 G. Ryan, A. Pandit and D. P. Apatsidis, *Biomaterials*, 2006, **27**, 2651.
6 H. Q. Nguyen, D. A. Deporter, P. M. Pilliar, N. Valiquette and R. Yakubovich, *Biomaterials*, 2004, **25**, 865.
7 J. P. Li, P. Habibovic, M. Doel van den, C. E. Wilson, J. R. Wijn de, C. A. Blitterswijk van and K. Groot de, *Biomaterials*, 2007, **28**, 2810.
8 J. D. Bobyn, R. M. Pilliar, H. U. Cameron and G. C. Weatherly, *Clin. Orthop. Relat. Res.*, 1980, **150**, 263.
9 S. A. Cho and K. T. Park, *Biomaterials*, 2003, **24**, 3611.
10 Y. T. Sul, C. B. Johansson, S. Petronis, A. Krozer, Y. Jeong, A. Wennerberg and T. Albrektsson, *Biomaterials*, 2002, **23**, 491.
11 D. Buser, T. Nydegger, T. Oxland, D. L. Cochran, R. K. Schenk, H. P. Hirt, D. Snétivy and L. P. Nolte, *J. Biomed. Mater. Res.*, 1999, **45**, 75.
12 D. M. D. Ehrenfest, P. G. Coelho, B. S. Kang, Y. T. Sul and T. Albrektsson, *Trends Biotechnol.*, 2010, **28**, 198.
13 Y. C. Tsui, C. Doyle and T. W. Clyne, *Biomaterials*, 1998, **19**, 2015.
14 C. K. Chang, J. S. Wu, D. L. Mao and C. X. Ding, *J. Biomed. Mater. Res.*, 2001, **56**, 17.
15 Y. Y. Yan, J. F. Sun, Y. Han, D. C. Li and K. Cui, *Surf. Coat. Tech.*, 2010, **205**, 1702.
16 H. Ishizawa, M. Fujino and M. Ogino, *J. Biomed. Mater. Res.*, 1997, **35**, 199.
17 Y. M. Wang, J. W. Guo, J. P. Zhuang, Y. B. Jing, Z. K. Shao, M. S. Jin, J. Zhang, D. Q. Wei and Y. Zhou, *Appl. Surf. Sci.* 2014, **299**, 58.
18 L. Xie, X. Liao, G. Yin, Z. Huang, D. Yan, Y. Yao, W. Liu, X. Chen and J. Gu, *J. Biomed. Mater. Res. A*, 2011, **98A**, 312.
19 L. Xie, X. Liao, H. Xu, G. Yin, Z. Huang, Y. Yao, X. Chen and J. Gu, *Mater. Lett.*, 2012, **72**, 141.
20 J. D. Bobyn, G. J. Wilson, D. C. MacGregor, R. M. Pilliar and G. C. Weatherly, *J. Biomed. Mater. Res.*, 1982, **16**, 571.
21 R. Zhou, D. Q. Wei, W. Feng, S. Cheng, H. Y. Yang, B. Q. Li, Y. M. Wang, D. C. Jia and Y. Zhou, *Surf. Coat. Technol.*, 2014, **252**, 148.
22 D. Krupa, J. Baszkiewicz, J. Zdunek, J. W. Sobczak, W. Lisowski, J. Smolik and Z. Slomka, *J. Biomed. Mater. Res. B*, 2012, **100**, 2156.
23 Y. Han, S. H. Hong and K. Xu, *Surf. Coat. Technol.*, 2003, **168**, 249.
24 W. H. Song, Y. K. Jun, Y. Han and S. C. Hong, *Biomaterials*, 2004, **25**, 3341.
25 D. Krupa, J. Baszkiewicz, J. Zdunek, J. Smolik, Z. Słomka and J. W. Sobczak, *Surf. Coat. Technol.*, 2010, **205**, 1743.
26 E. J. Lee, D. S. Shin, H. E. Kim, H. W. Kim, Y. H. Koh and J. H. Jang, *Biomaterials*, 2009, **30**, 743.
27 Y. Chen, X. Zheng, H. Ji and C. Ding, *Surf. Coat. Technol.*, 2007, **202**, 494.
28 P. Zhang, Z. G. Zhang, W. Li and M. Zhu, *Appl. Surf. Sci.*, 2013, **268**, 381.
29 H. J. Song, J. W. Kim, M. S. Kook, W. J. Moon and Y. J. Park, *Appl. Surf. Sci.*, 2010, **256**, 7056.
30 F. Xiao, K. Tsuru and A. Hayakawa Osaka, *Thin Solid Films*, 2003, **441**, 271.
31 X. X. Wang, S. Hayakawa, K. Tsuru and A. Osaka, *Biomaterials*, 2002, **23**, 1353.
32 X. Y. Liu, X. B. Zhao, B. E. Li, C. Cao, Y. Q. Dong, C. X. Ding and P. K. Chu, *Acta Biomater.*, 2008, **4**, 544.
33 A. Oyane, H. M. Kim, T. Furuya, T. Kokubo, T. Miyazaki and T. Nakamura, *J. Biomed. Mater. Res. A*, 2003, **65A**, 188.
34 A. L. Yerokhin, L. O. Snizhko, N. L. Curevina, A. Leyland, A. Pilkington and A. Matthews, *J. Phys. D: Appl. Phys.* 2003,**36**, 2110.
35 X. Ping, S. B. Zhang, J. L. You, G. C. Jiang, H. Chen and H. Zeng, *Spectrosc. Spect. Anal.*, 2007, **27**, 936.
36 S. Cheng, D. Q. Wei, Y. Zhou and H. F. Guo, *Ceram. Int.*, 2011, **37**, 2505.
37 A. Dupraz, T. P. Nguyen, M. Richard, G. Daculsi and N. Passuti, *Biomaterials*, 1999, **20**, 663.
38 R. Zhou, D. Q. Wei, S. Cheng, B. Q. Li, Y. M. Wang, D. C. Jia, Y. Zhou and H. F. Guo, *Ceram. Int.*, 2014, **40**, 501.
39 T. E. Madey, C. D. Wagner and A. Joshi, *J. Electron Spectrosc. Relat. Phenom.*, 1977, **10**, 359.
40 B. D. Ng, I. Annergren, A. M. Soutar, K. A. Khor and A. E. W. Jarfors, *Biomaterials*, 2005, **26**, 1087.
41 Y. Han, D. H. Chen, J. F. Sun, Y. M. Zhang and K. W. Xu, *Acta Biomater.*, 2008, **4**, 1518.
42 C. Viornery, Y. Chevolot, D. Léonard, B.O. Aronsson, P. Péchy, H. J. Mathieu, P. Descouts and M. Grätzel, *Langmuir*, 2002, **18**, 2582.
43 T. K. Sham and M. S. Lazarus, *Chem. Phys. Lett.*, 1979, **68**, 426.
44 F. M. F. de Groot, M. Grioni and J. C. Fuggle, *Phys. Rev. B*, 1989, **40**, 5715.
45 T. Kasuga, H. Kondo and M. Nogami, *J. Cryst. Growth*, 2002, **235**, 235.
46 R. Camposeco, S. Castillo, I. Mejia, V. Mugica, R. Carrera, A. Montoya, M. Morán-Pineda, J. Navarrete and R. Gómez, *Catal. Commun.*, 2012, **17**, 81.
47 M. T. Kim, *Thin Solid Films*, 1997, **311**, 157.
48 B. L. Su and V. Norberg, *Zeolites*, 1997, **19**, 65.
49 L. Müller and F. A. Müller, *Acta Biomater.*, 2006, **2**, 181.
50 Z. F. Liu, W. Q. Wang, H. Y. Liu, T. Y. Wang and M. Qi, *Appl. Surf. Sci.*, 2013, **266**, 250.
51 R. Zhou, D. Q. Wei, S. Cheng, Y. Zhou, D. C. Jia, Y. M. Wang and B. Q. Li, *Ceram. Int.*, 2013, **39**, 5725.
52 S. Tsunekawa, Y. Aoki and H. Habazaki, *Surf. Coat. Technol.*, 2011, **205**, 4732.
53 M. M. Lohrengel, *Mater. Sci. Eng. R-Rep.*, 1993, **11**, 243.
54 E. Matykina, R. Arrabal, P. Skeldon and G. E. Thompson, *Acta Biomater.*, 2009, **5**, 1356.